Original Article | Journal of Biosystems Engineering

J. of Biosystems Eng. 39(3):166-173. (2014. 9)
http://dx.doi.org/10.5307/JBE.2014.39.3.166

eISSN : 2234-1862
pISSN : 1738-1266

Multispectral Wavelength Selection to Detect 'Fuji' Apple Surface Defects with Pixel-sampling Analysis

Soo Hyun Park[1,3], Hoyoung Lee[2], Sang Ha Noh[1]*

[1]*Department of Biosystems & Biomaterials Science and Engineering, Seoul National University, Seoul, 151-921, Korea*
[2]*Environmental Microbiology and Food Safety Laboratory, Animal and Natural Resources Institute, Agricultural Research Service, U.S. Department of Agriculture, Powder Mill Rd. Bldg 303, BARC-East, Beltsville, MD 20705, U.S.A.*
[3]*Research Institute for Agriculture and Life Sciences, Seoul National University, Seoul, 151-921, Korea*

Received: June 18th 2014; Revised: July 20th 2014; Accepted: August 20th 2014

Abstract

Purpose: In this study, we focused on the image processing method to determine the external quality of Fuji apples by identifying surface defects such as scabs and bruises. **Method:** A CCD camera was used to capture filter images with 24 different wavelengths ranging between 530 nm and 1050 nm. Image subtraction and division operations were performed to distinguish the defect area from the normal areas including calyx, stem, and glaring on the apple surface image. All threshold values of the image were examined to reveal the defect area of pretreated filter images. **Results:** The developed operation methods were [image (720 nm) − image (900 nm)]/image (700 nm) for bruise detection and [image (740 nm) − image (900 nm)]/image (590 nm) for scab detection, which revealed 81% and 90% recognition ratios, respectively. **Conclusions:** Our results showed several optimal wavelengths and image processing methods to detect Fuji apple surface defects such as bruises and scabs.

Keywords: Apple bruise, Apple scab, Image process, Pixel sampling analysis, Surface defect

Introduction

Visible/near-infrared spectroscopy is commonly used to analyze material composition or to evaluate localized features such as internal/external defects (Windham *et al.*, 2003). Properties of light absorption and scattering information are used to examine internal properties of agricultural products and physical/spatial information of defects. The information regarding surface defects on a sample can be determined with a normal charge-coupled device (CCD) camera and image-processing methods; however, these methods have the added complexity of identifying features that are localized rather than systemic to the whole object. Furthermore, conventional imaging instrumentation lacks the ability to measure material composition through spectral analysis (Lee *et al.*, 2008).

Surface defect detection is of great concern to apple farmers as perceived quality is related to the appearance, and an existence of surface defects is an important quality index to consumers (Lu, 2003; Röhr *et al.*, 2005). It is a great concern to separate the damaged from the sound, but screening apples for surface defects is mainly performed by hand, even though numerous studies have been conducted and commercial machinery is available. Distinguishing between stem/calyx and defects has not yet been achieved; hence the need to orient the apples in order to keep the stem/calyx out of the images (Bennedsen and Peterson, 2005). Several researchers have attempted to address this problem with varying degrees of success (Crowe and Delwiche, 1996), achieving error rates between 9% and 33%. This wide error range is the reason why the system cannot be used in its current configuration to detect defects in the stem/calyx area. However, according to the

***Corresponding author:** Sang Ha Noh
Tel: +82-2-880-4603; **Fax:** +82-2-873-2049
E-mail: noh@snu.ac.kr

concept described by Throop *et al.* (2000), orienting the apples allows the use of additional cameras to specifically inspect the stem and calyx region (Throop and Aneshansley, 1997). Hence, with more cameras, three sets of images can be acquired for each apple: one covering the stem region, another the calyx region, and a number of images covering the circumference as the apple rotates (Bennedsen and Peterson, 2005). Additional cameras increase the equipment cost; therefore, further research is needed in order to design a method for inspecting the stem/calyx area without the need for installing additional cameras.

In a recent study, a hyperspectral camera as a supplement to the existing instruments and methods combined the complementary approaches of spectral analysis and image processing to allow the potential for defect recognition and quantification (Xing *et al.*, 2005; Lu, 2007; ElMasry *et al.*, 2008). Although technologically advanced, such technology is currently not feasible for several reasons. First, hyperspectral imaging is too costly for examining an apple surface. Second, the imaging is too slow to be applied to an online vision system for apple grading because tremendous amounts of spectral and spatial data are required. This is the reason why hyperspectral imaging has often been used as a precursor to online multispectral machine vision systems in recent studies (Lee *et al.*, 2008; Lee *et al.*, 2014). Upon identification of meaningful wavelengths through hyperspectral image analysis, the two to four most important wavelengths can be packaged in a dedicated multispectral image analysis inspection system. Key to this process in hyperspectral analysis is the selection procedure for identifying the wavelengths.

The objective of this study was to develop an image-processing method and to identify the two to three optimum wavelengths for use in a multispectral system capable of detecting defects in apples during online grading.

Materials and Methods

Apples

Fuji apple samples from an orchard in Gyeongbuk province, South Korea, were purchased at the local market. A total of 50 apples with visible surface scabs were randomly selected for image acquisition. Additionally, ten apples without surface defects were also selected, and their surfaces were damaged with a wooden spoon in order to cause bruising. The bruise marks appeared with a diameter of less than 10 mm and a depth of less than 3 mm. Most of the bruises were verified that they were similar to uncontrolled bruises by showing the typical browning symptoms. The total number of defects was 200, and the majority of apples had at least one defect region such as a bruise or a scab. Prior to filter image acquisition, a digital camera captured the sample surfaces to assist in identifying defects.

Image acquisition system

The Visible/Near Infrared (Vis/NIR) imaging system as shown in Figure 1 was composed of a CCD camera (Model: KF-F2A, Hitachi, Japan), a filter wheel attached to the camera lens, two 150 W halogen A-line lightbulb lamps (Osram, Germany), a cylindrical diffuser manufactured with a white acryl board and a PC with frame grabber card. A total of nine band-pass filters were mounted on the wheel, which had 24 different wavelengths interposed with 20 nm intervals between 530 and 1000 nm, as well as 1050 nm. The wheel with the mounted band-pass filters was designed to prevent position shifting and allow for zoom-in and zoom-out between images, and the diffuser was installed to minimize glare.

Image acquisition was performed with all prepared samples using a PCI-1411 frame grabber (National Instruments, Austin, USA) and IMAQ software (National Instrument Corporation, Austin, USA), and the image processing was performed by hand-coded software that was developed in DEV-C++ (Bloodshed Software). Since transmittance of each wavelength was different, NIR images were grabbed by adjusting the lens iris so that similar gray-level images could be obtained. To reduce the noise and image calculation,

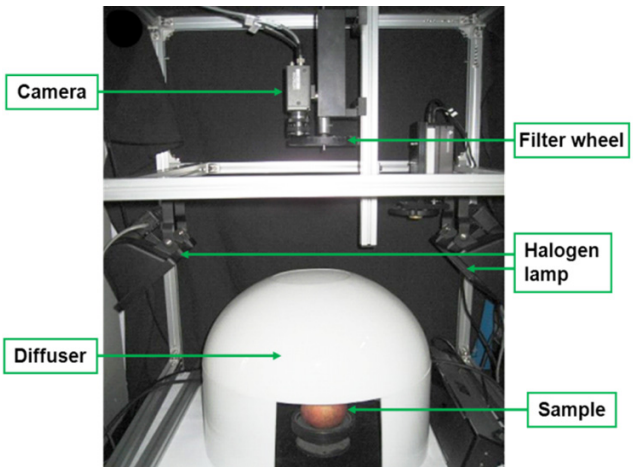

Figure 1. Vis/NIR filter image acquisition system.

the image was convoluted with a 3 x 3 smoothing filter and was down-sampled four times, resulting in dimensions of 320 x 240.

Image processing and data analysis method

The acquired filter image background was eliminated by equation 1, and the image set region of interest (ROI) was obtained as shown in Figure 2(b) and (e). The ROI mask representing the selected apple subset area in the image was segmented by a labeling algorithm. The image was normalized using equation 2, as shown in Figure 2(c) and (f), and was analyzed for the mean, minimum, and maximum values obtained from the ROI masked image. The image set brightness for each sample was equivalent because the mean of every normalized image was set to 128, and the minimum and maximum of the normalized images were set to the minimum and maximum, respectively, of the original image set. Figure 2 shows the process for obtaining the normalized image with two wavelength-filtered images of 700 nm and 1000 nm. Scabs shown in Figure 2(a) are more evident in the 700 nm filter image, while they appear darker in the 1000 nm filter image, as shown in Figure 2(d). In addition, the area around the stem is more evident in the 700 nm filter image compared to the 1000 nm image.

$$IMG_{nobg}(x,y) = \begin{pmatrix} 0 & if\ \ IMG_{org}(x,y) < T \\ IMG_{org}(x,y) & IMG_{org}(x,y) \geq T \end{pmatrix} \quad (1)$$

where $IMG_{nobg}(x,y)$ = background removal image
$IMG_{org}(x,y)$ = original image
T = threshold value

$$IMG_{nor}(x,y) = \begin{pmatrix} 128/(M-Min)*(IMG_{org}(x,y)-Min) & if\ \ IMG_{org}(x,y) < M \\ 128/(Max-M)*(IMG_{org}(x,y)-M)+128 & if\ IMG_{org}(x,y) \geq M \end{pmatrix} \quad (2)$$

where $IMG_{nor}(x,y)$ = normalized image
$IMG_{org}(x,y)$ = original image
M = mean of image
Min = minimum of image set
Max = maximum of image set

The randomly sampled pixels of the normalized image were classified as Normal Surface (NS), Glaring Normal Surface (GNS), Cross-section of Stalk (CS), Stem (S), Around Stem (AS), Calyx (C), Calyx Hole (CH), Strong Bruise (SB), Weak Bruise (WB), Brown Scab (BS1), and Black Scab (BS2), and the number of selected pixels was 745, 553, 129, 57, 93, 195, 51, 198, 324, 257, and 75, respectively. The sampling details are presented in Figure 3.

All sampling points were collected and used to plot the average spectra by wavelength in order to investigate the differences among parts. In order to distinguish clearly between the defective and sound parts, an image algorithm was employed. The algorithm method flow chart is shown in Figure 4. All sampled points were classified as either

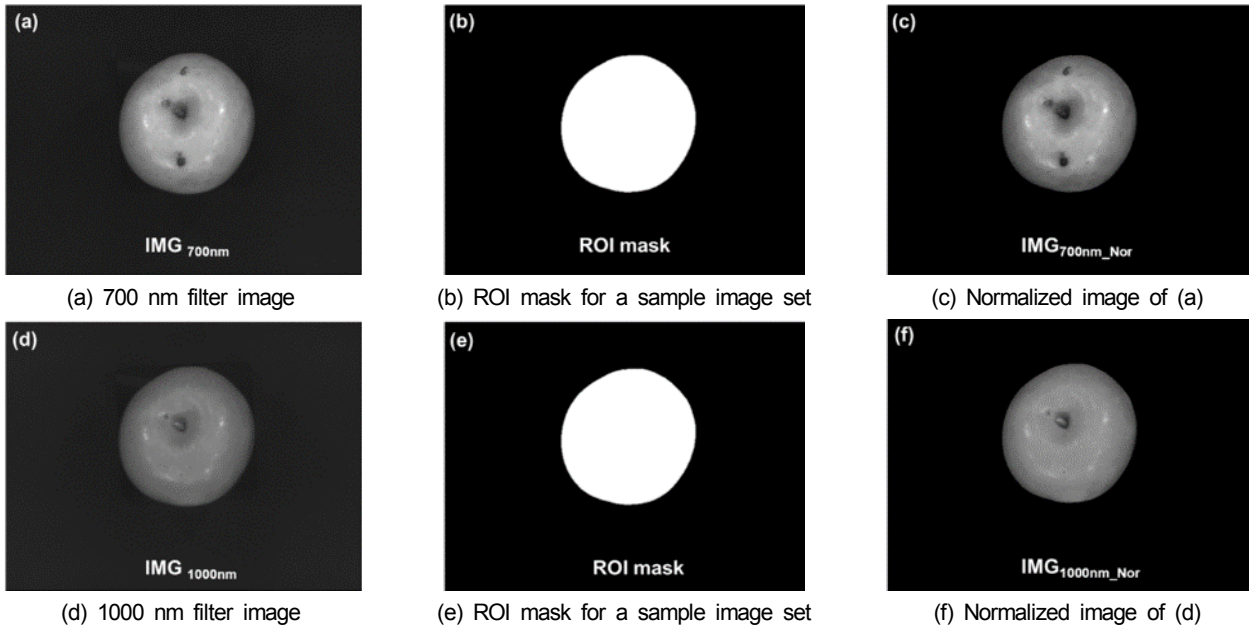

(a) 700 nm filter image (b) ROI mask for a sample image set (c) Normalized image of (a)

(d) 1000 nm filter image (e) ROI mask for a sample image set (f) Normalized image of (d)

Figure 2. ROI mask features and image normalization to filter image.

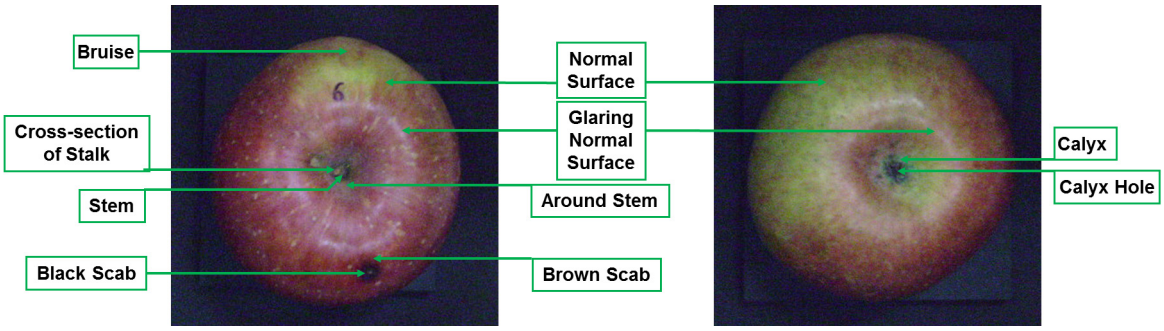

Figure 3. Pixel sampling locations and names of apple parts.

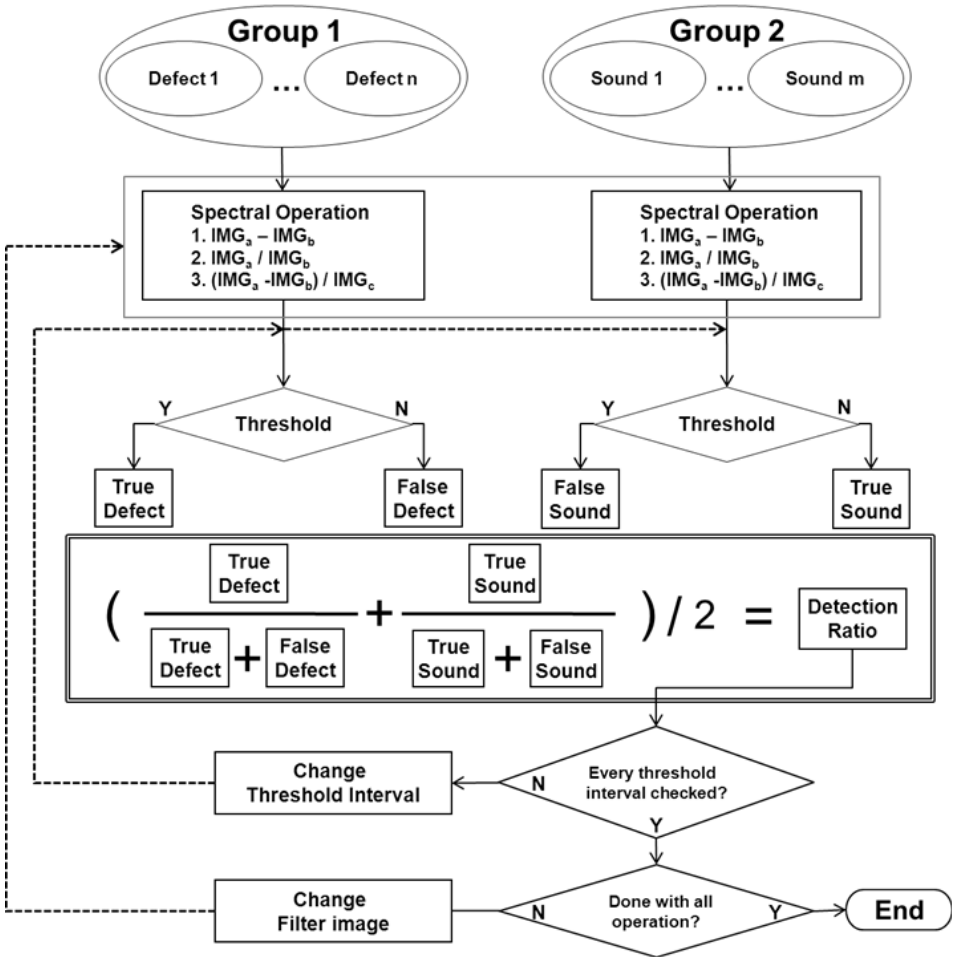

Figure 4. Algorithm to determine operation type, optimal image wavelengths, threshold interval, and maximum detection ratio of each step for scab and bruise detection.

defective or sound. All parts except for SB and WB were defined as sound parts when the bruise detection was calculated. Likewise, all parts except for BS1 and BS2 were defined as sound parts when scab detection was calculated. Every up-cut and down-cut value as end-values of the multi-thresholding process was determined to discriminate between defective and sound parts on the image using subtraction, division, and a mixture of subtraction and division. Then, the number of true or false determination results was used to calculate the detection ratio. The up-cut and down-cut threshold values, operation, and wavelengths used in the filtered images were calculated when the detection ratio was the highest according to operation.

Results and Discussion

Figure 5 illustrates the average spectra of gray level at every classified part on a Fuji apple. The spectra data were extracted from filter images at sampling points, whereupon averaging was performed to plot a graph so that the unique wavelength band could be highlighted to discriminate between parts. A dominant spectral feature observed in AS and CH was a gray level value lower than in other parts, demonstrating that reflective light was less due to the recessed configuration. In addition, a slight change appeared at 650 nm in a few parts; however, most parts showed a monotonic increase at 700 nm.

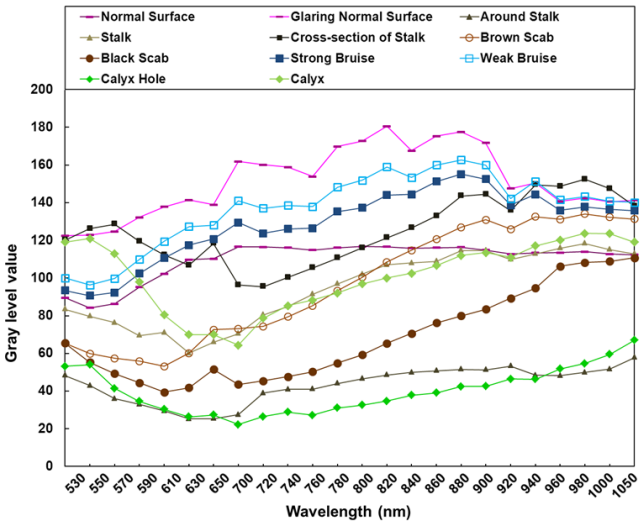

Figure 5. Average gray level spectra at each part.

Although numerous attempts to detect surface defects of the Fuji apple with image processing have been performed, the stem-end and calyx areas were often identified erroneously as a defect. For that reason, Xing *et al.* (2007) and Zhang *et al.* (2012) attempted to discriminate stem-end and calyx from defects, and have achieved a remarkable result of over 95% detection ratio. In this study, we attempted a new method to detect bruises and scabs on apple surfaces despite the presence of the stem, calyx, and glares in the images.

The detection ratio when a single operation was performed with two filter images is shown in Figure 6. The maximum ratio for detecting a scab was observed when the division operation was performed with 610 nm and 980 nm

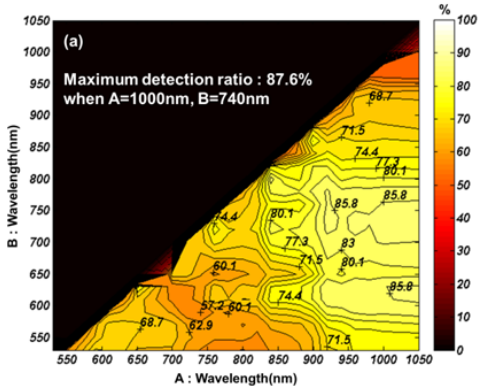

(a) Scab detection, operation: subtraction (B − A)

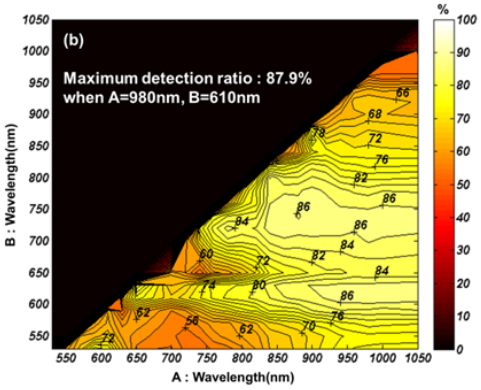

(b) Scab detection, operation: division (B / A)

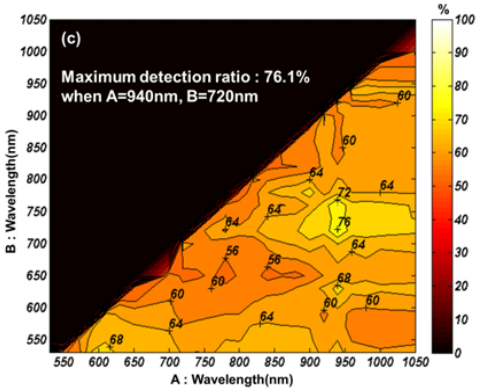

(c) Bruise detection, operation: subtraction (B − A)

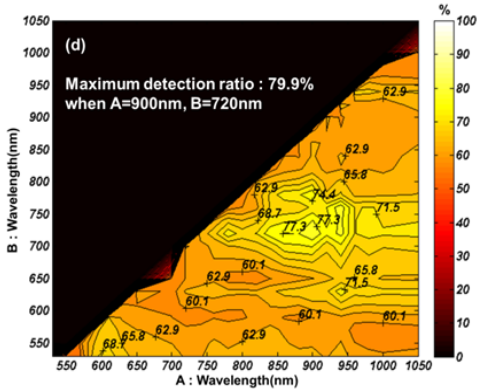

(d) Bruise detection, operation: division (B / A)

Figure 6. Contour plot of detection ratio.

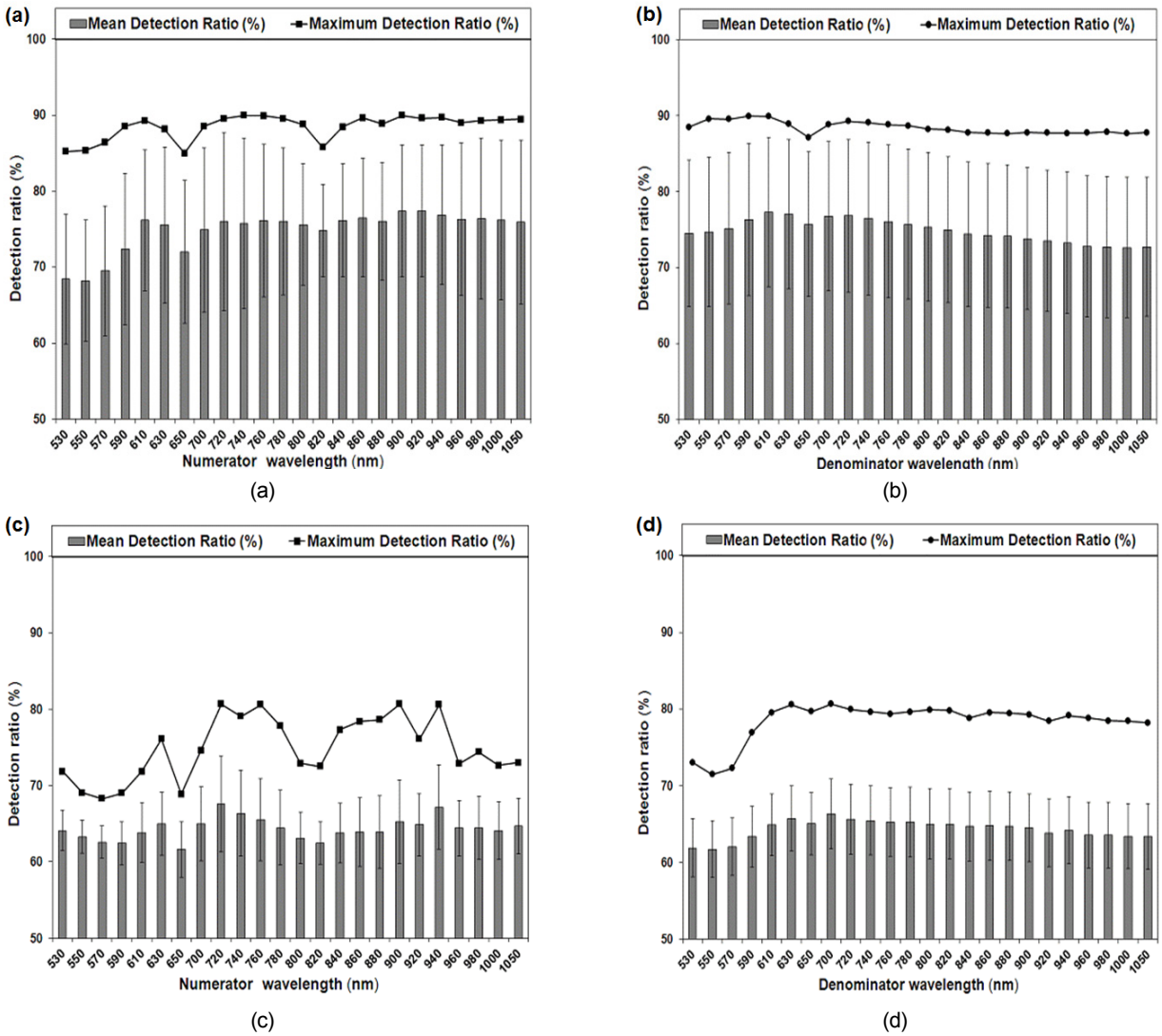

Figure 7. Detection ratio change according to numerator and denominator wavelengths for scab (a and b) and bruise (c and d).

images. The detection rate when the subtraction operation was performed with 740 nm and 1000 nm showed similar results. When operations for bruise detection were executed, the maximum detection ratio was observed with the division operation in the 720 nm and 900 nm images. This suggests that scab detection is easier than bruise detection, and the division operation is more appropriate to discriminate defects.

The detection ratio when $(IMG_a - IMG_b) / IMG_c$ was performed with three filter images is shown in Figure 7 according to numerator and denominator wavelengths. Since every single value was investigated as up-cut or down-cut in a multi-threshold process, the detection ratio was extremely low, close to 0%, when close values were selected as up-cut and down-cut. That led to large standard deviation ranges of mean detection ratio, however, we only focused on finding the highest detection ratio. Generally, scab detection shows better performance compared to bruise detection, demonstrating a more improved detection ratio when the wavelength is used as the numerator compared to when the wavelength is used as the denominator. Thus, it is determined that careful selection of the numerator's wavelength is needed.

In order to investigate which spectral wavelength affects the detection ratio with a fixed denominator wavelength, the contour plots of the detection ratio were constructed when two $(IMG_a - IMG_b) / IMG_c$ operations were performed, as shown in Figure 8. The maximum detection ratio was observed when 590 nm and 700 nm were used as the denominator to detect scab and bruise, respectively.

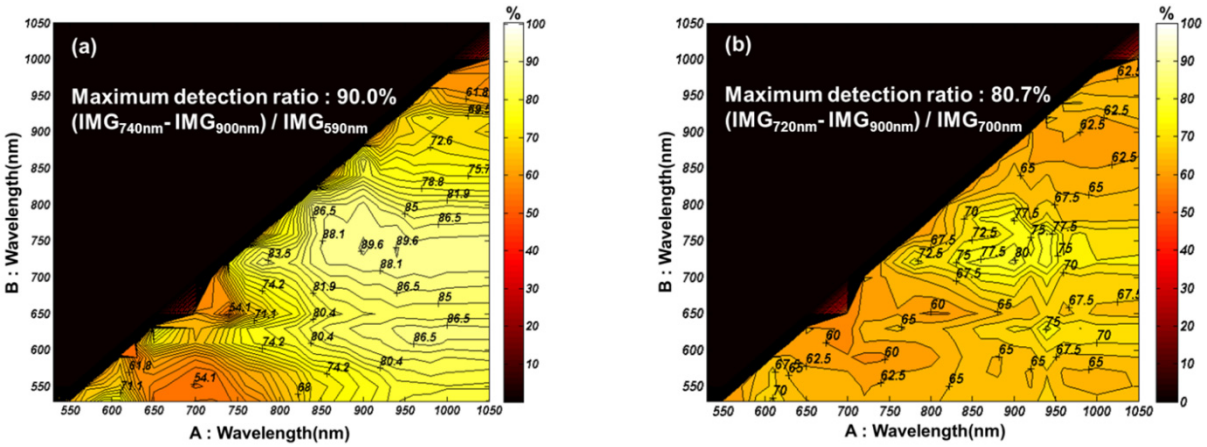

(a) Scab detection ratio when (B − A) / IMG_{590nm} is performed (b) Bruise detection ratio when (B − A) / IMG_{700nm} is performed

Figure 8. Contour plot of detection ratio when a mixture of operations is performed.

Table 1. Maximum detection ratio and selected wavelengths according to operation

	Operation	Up-cutDetection	Down-cut	Detection ratio (%)	Wavelengths of filter images
Scab	IMG_a - IMG_b	−255	−24	87.6076	a = 740 nm, b = 1000 nm
	IMG_a / IMG_b	1242	5542	87.9018	a = 610 nm, b = 980 nm
	(IMG_a − IMG_b) / IMG_c	−2550000	−4847	89.9873	a = 740 nm, b = 900 nm, c = 590 nm
Bruise	IMG_a − IMG_b	−39	−5	76.1421	a = 720 nm, b = 940 nm
	IMG_a / IMG_b	7017	9137	79.8991	a = 720 nm, b = 900 nm
	(IMG_a − IMG_b) / IMG_c	−3903	−682	80.7035	a = 720 nm, b = 900 nm, c = 700nm

The overall meaningful results are shown in Table 1, which includes the maximum detection ratio, multi-threshold values, and optimal wavelengths for scab and bruise detection. Compared with other operations, (IMG_a − IMG_b) / IMG_c showed a higher detection ratio. The developed operation methods and optimal wavelengths were (IMG_{740nm} − IMG_{900nm}) / IMG_{590nm} for scab detection and (IMG_{720nm} − IMG_{900nm}) / IMG_{700nm} for bruise detection, which revealed 90% and 81% recognition ratios, respectively.

The aim of multispectral wavelength selection is to determine two or three wavelength bands of filter images, type of operation, and threshold values. An advantage of the multispectral division compared to subtraction is that spatial responses across a sample can be normalized (Lee *et al.*, 2008). The detection ratio of the division operation showed better performance in detecting scabs and bruises than the subtraction operation. Additionally, the mixed operation method showed a higher detection ratio than the single operation, suggesting that three wavelength selections are superior to two wavelengths for detecting defects on a Fuji apple surface.

Conclusion

In this study, pixel-sampling analysis was performed in order to develop the image-processing method, and to identify the several wavelengths used in a multispectral system capable of detecting defects such as scabs and bruises in Fuji apples. We attempted to detect bruises and scabs pixels despite the presence of the stem, the calyx, and glare pixels in the images. Although an applicable wavelength to classify defects in an image was not present on the average gray level spectra, several bands were found when subtraction, division, and mixed operations were performed. The maximum detection ratio was observed with a mixed operation performed to detect both scabs and bruises, whereupon the 590 nm, 740 nm, and 900 nm and 700 nm, 720 nm, and 900 nm wavelength sets were determined for scab and bruise detection, respectively. The developed operation methods and optimal wavelengths were (IMG_{740nm} − IMG_{900nm}) / IMG_{590nm} for scab detection and (IMG_{720nm} − IMG_{900nm}) / IMG_{700nm} for bruise detection, which revealed 90% and 81% recognition ratios, respectively.

The benefit of selecting two or three wavelength filters compared to hyperspectral imaging is the speed of analysis and apple measurement, in addition to less expensive online sorting. Therefore, considering that our results showed several optimal wavelengths and image-processing methods to detect Fuji apple surface defects such as bruises and scabs, it shows its potential for use with fast, non-destructive processing operation methods to ensure food quality, increase efficiency, and reduce costs.

Conflict of Interest

The authors have no conflicting financial or other interests.

Acknowledgement

The authors would like to extend their appreciation to all members in Biosystems Control and Automation Laboratory at Seoul National University. JongWoo Ha, XiongZhe Han, Dae-Hyun Jung, HeeSup Yun, and ByungChang Kim contributed their insightful comments on this work and generously provided useful references to identify the deficiencies in this paper.

References

Bennedsen, B. S and D. L. Peterson. 2005. Performance of a system for apple surface defect identification in near-infrared images. Biosystems Engineering 90(4): 419-431.

Crowe, T. G and M. J. Delwiche. 1996. Real-time defect detection in fruit-Part I: Design concepts and development of prototype hardware. Transactions of the ASAE 39(6):2299-2308.

ElMasry, G., Wang, N., Vigneault, C., Qiao, J and A. ElSayed. 2008. Early detection of apple bruises on different background colors using hyperspectral imaging. LWT-Food Science and Technology 41(2):337-345.

Lee, K., Kang, S., Delwiche, S. R., Kim, M. S and S. H. Noh. 2008. Correlation analysis of hyperspectral imagery for multispectral wavelength selection for detection of defects on apples. Sensing and Instrumentation for Food Quality and Safety 2(2):90-96.

Lee, H., Yang, C. C., Kim, M. S., Lim, J., Cho, B. K., Lefcourt, A., Chao, K and C. D. Everard. 2014. A simple multispectral imaging algorithm for detection of defects on red delicious apples. Journal of Biosytems Engineering 39(2):142-149.

Lu, R. 2003. Detection of bruises on apples using near-infrared hyperspectral imaging. Transactions-American Society of Agricultural Engineers 46(2):523-530.

Lu, R. 2007. Nondestructive measurement of firmness and soluble solids content for apple fruit using hyperspectral scattering images. Sensing and Instrumentation for Food Quality and Safety 1(1):19-27.

Röhr, A., Lüddecke, K., Drusch, S., Müller, M. J and R. V. Alvensleben. 2005. Food quality and safety—consumer perception and public health concern. Food Control 16(8):649-655.

Throop, J. A and D. J. Aneshansley. 1997. Apple damage segmentation utilizing reflectance spectra of the defect. ASEA paper 97-3078. St. Joseph, MI: ASAE.

Throop, J. A., Aneshansley, D. J and B. Anger. 2000. Multispectral inspection station detects defects on apples. In: *Environmental and Industrial Sensing*, pp. 37-46. Boston, MA: International Society for Optics and Photonics.

Windham, W. R., Lawrence, K. C., Park, B and R. J. Buhr. 2003. Visible/NIR spectroscopy for characterizing fecal contamination of chicken carcasses. Transactions of the ASAE 46(3):747-751.

Xing, J., Jancsók, P and J. Baerdemaeker. 2007. Stem-end/calyx identification on apples using contour analysis in multispectral images. Biosystems Engineering 96(2):231-237.

Xing, J., van Linden, V., Vanzeebroeck, M and J. Baerdemaeker. 2005. Bruise detection on Jonagold apples by visible and near-infrared spectroscopy. Food Control 16(4): 357-361.

Zhang, C., Chen, L., Huang, W., Guo, Z and Q. Wang. 2012. Apple stem-end/calyx identification using a speckle-array encoding pattern. In *Signal Processing (ICSP), 2012 IEEE 11th International Conference*. Vol. 2, pp. 1110-1114. Beijing: IEEE.